J. Space Weather Space Clim. 2022, **12**, 39

https://doi.org/10.1051/swsc/2022037

JSWSC

Available online at:
www.swsc-journal.org

RESEARCH ARTICLE OPEN ACCESS

A statistical study of polar cap flow channels observed in both hemispheres using SuperDARN radars

Katie Herlingshaw[1,2,*], Lisa Baddeley[1,2], Kjellmar Oksavik[1,2], Dag A. Lorentzen[1,2], and Karl M. Laundal[1,2]

[1] Department of Arctic Geophysics, University Centre in Svalbard, Longyearbyen 9171, Norway
[2] Birkeland Centre for Space Science, University of Bergen, Bergen 5007, Norway

Received 19 April 2022 / Accepted 29 October 2022

Abstract – This paper details the first large-scale, interhemispheric statistical study into ionospheric fast flow (>900 m/s) channels in the polar cap using the SuperDARN radar network. An automatic algorithm was applied to 6 years of data (2010–2016) from 8 SuperDARN radars with coverage in the polar cap regions in both hemispheres. Over 17,000 flow channels were detected, the majority of which occurred in the dayside polar cap region. To determine a statistical relationship between the flow channels and the IMF, a Monte Carlo simulation was used to generate probability distribution functions for IMF conditions and dipole tilt angles. These were used as a baseline for comparisons with IMF conditions associated with the flow channels. This analysis showed that fast flow channels are preferentially driven by IMF B_y dominant conditions, suggesting that a magnetic tension force on the newly reconnected field lines is required to accelerate the ionospheric plasma to high speeds on the dayside. The flow channels also occur preferentially during disturbed IMF conditions. Large populations of flow channels were observed on the flanks of the polar cap region. This indicates that significant momentum transfer from the magnetosphere can routinely occur on open field lines on the flanks, far from the dayside and nightside reconnection regions.

Keywords: Ionospheric flow channels / Ionospheric convection / Solar wind driving conditions

1 Introduction

On a large scale, the high latitude ionosphere circulates in a twin-cell convection pattern for a southward interplanetary magnetic field (IMF) (Dungey, 1961, 1963) geophysics. Magnetic flux circulates from the dayside due to reconnection between the IMF and Earth's magnetic field, moving antisunwards over the polar caps on open field lines, then reconnecting in the magnetotail to form sunward convecting closed field lines. If a positive IMF B_y (negative IMF B_y) component is present, in the Northern Hemisphere the dusk (dawn) cell will appear round and dominate over the crescent-shaped dawn (dusk) cell (Heelis, 1984; Burch et al., 1985; Lu et al., 1994; Rich & Hairston, 1994). The opposite sense is true in the Southern Hemisphere. The response of large-scale convection to different solar wind/IMF conditions has been encapsulated well in statistical models (Heppner, 1977; Heppner & Maynard, 1987; Ruohoniemi & Greenwald, 1996, 2005; Cousins & Shepherd, 2010; Pettigrew et al., 2010).

However, in recent years it has been shown that mesoscale fast-flowing features (100–500 km) frequently occur in the magnetosphere–ionosphere system (Lyons et al., 2016). These features are not adequately described by the large-scale statistical models of ionospheric convection, despite the fact that they can account for substantial amounts (10–60%) of the polar cap potential, which suggests they are important in the transportation of magnetic flux over the polar cap (Andalsvik et al., 2011; Zou et al., 2015; Herlingshaw et al., 2019). The mesoscale flow events are defined differently depending on the type of data (e.g. optical or radar) and the location in which they are observed, but are generally described as fast-flowing mesoscale features embedded in the slower-moving background convection.

Pinnock et al. (1993) observed a longitudinally elongated (>900 km), latitudinally narrow (100 km), high velocity (2–3 km/s) signature in Polar Anglo-American Conjugate Experiment (PACE) HF radar data and named the structure a flow channel event (FCE). These signatures were discovered to be the ionospheric response to flux transfer events (FTEs) (Neudegg et al., 2000), which are bursts of reconnection at the dayside magnetopause with a mean periodicity of 8 min (Haerendel et al., 1978; Russell & Elphic, 1978, 1979; Lockwood & Wild, 1993). This category of flow channels was further researched by Provan et al. (1998), who noted a

*Corresponding author: katieh@unis.no

pulsing in the flow channels with a similar periodicity to FTEs, terming them pulsed ionospheric flows (PIFs). An IMF B_y dependency on PIFs was noted in a 2-year statistical survey of SuperDARN radar data (Provan et al., 1999). In the Northern Hemisphere, the PIF location was noted to shift towards post-noon (prenoon) for positive IMF B_y (negative IMF B_y) with a westward (eastward) flow direction. This suggests these flows are strongly driven by the magnetic field tension effects associated with IMF B_y. This was shown statistically by Herlingshaw et al. (2020), using 2 years of data from the SuperDARN Longyearbyen radar. However, as only one radar was used in this study, it could not be proven that the result was not due to the zonally directed radar preferentially detecting the azimuthal flows associated with IMF B_y.

Flow channels have also been observed on the dawn/dusk flanks of the polar cap (Farrugia et al., 2004; Sandholt & Farrugia, 2007, 2009; Oksavik et al., 2010; Sandholt et al., 2010; Andalsvik et al., 2011; Nishimura et al., 2014), on the nightside (Lyons et al., 2011; Gallardo-Lacourt et al., 2014; Zou et al., 2014; Gabrielse et al., 2018) and within the sunward return flow on closed field lines (Lockwood et al., 1993; Moen et al., 1995, 2006). To examine the evolution of flow channels at different stages during the Dungey cycle, different categories of flow channels have been developed, known as FC 0, FC 1, FC 2, FC 3, and FC 4. This work was mainly carried out by Sandholt and Farrugia (2009), and therefore will be referred to as the S&F framework throughout this paper. FC 1 and FC 2 represent dayside-driven flow channels at different stages in their evolution (Sandholt et al., 2004; Sandholt & Farrugia, 2009; Andalsvik et al., 2011). FC 1 occurs within 10 min of reconnection at the dayside on newly opened field lines in the vicinity of the open-closed boundary and includes features such as FCEs and PIFs. FC 2 are classified as flow channels on "old open field lines", which reconnected 10–20 minpreviously and include the narrow flow channels observed on the dawn and dusk flanks by Sandholt and Farrugia (2009). They argue that significant momentum transfer can be present on old open field lines that are connected to dynamo action in the high-latitude boundary layer tailward of the cusp, which maps to flow channels on the dawn and the dusk flank (06–09/15–18 magnetic local time) dependent on the sign of IMF B*y*. FC 3 and FC 4 are nightside-driven flow channels with field lines connected to the tail lobe and plasma sheet respectively. FC 3 flows occur on old open field lines located immediately poleward of the nightside auroral oval and are related to substorm activity and the closure of lobe flux during magnetotail reconnection (Wang et al., 2010). FC 4 is associated with westward electrojet enhancements, auroral streamer events (Sergeev et al., 1996), and poleward boundary intensifications in the aurora due to processes such as bursty bulk flows (Birn et al., 2011). Lastly, FC 0 is associated with flow channels on closed field lines in the return flow at subauroral latitudes on the equatorward side of evening auroral arcs (Marklund, 1984; Sandholt & Farrugia, 2009).

There have been many case studies of flow channels, and statistical studies of one particular type of flow channel or a select range of magnetic local times. How exactly the flow channels develop from stage to stage, especially on their journey over the polar cap, is still an open research question. In particular, the extent and occurrence of FC 2 have not been statistically examined. In this study, we use a flow channel detection algorithm on 6 years of SuperDARN data obtained by radars within the polar region in both the Northern and Southern Hemispheres. We concentrate on very fast-flowing channels (>900 m/s), as these are the times of strongest coupling between the solar wind and the magnetosphere–ionosphere system, where the most momentum and flux will be transported. The statistical occurrence distribution of the flow channels is discussed, as is the relationship between the flow channels and their solar wind-driving conditions.

2 Method and instrumentation

2.1 Super Dual Auroral Radar Network (SuperDARN)

The Super Dual Auroral Network (SuperDARN) is an international chain of high-frequency coherent scatter radars (Greenwald et al., 1995; Chisham et al., 2007; Nishitani et al., 2019). Their primary purpose is to record the $E \times B$ plasma flow in the F-region ionosphere over large areas within their fields of view (2500 km range, 52° azimuth). The radars are frequency agile, with a bandwidth of 8–20 MHz, and they routinely measure the line-of-sight Doppler velocity, backscatter power, and spectral width from decameter-scale ionospheric irregularities. Each radar field-of-view used is divided into 16 azimuthally consecutive beams separated by 3.25° increments, and each beam is divided into 75 range gates of 45 km resolution. Not all radars conform to this configuration, but it is true for the radars used in this study. We use data from Clyde River (CLY), Inuvik (INV), Rankin Inlet (RKN), and Longyearbyen (LYR) in the Northern Hemisphere. In the Southern Hemisphere, we use data from McMurdo (MCM), South Pole Station (SPS), Zhongshan (ZHO), and Dome C (DCE). The radar locations and fields-of-view are shown in Figure 1 and the fields-of-view are shaded in the 1/2 hop F-region, as this is where most flow channels occur due to the detection method (Section 2.2) and radar propagation conditions. The regions are colored based on orientation, where green and blue colors represent mostly zonally and meridionally orientated regions respectively. Further information such as the radar's name, station ID, hemisphere, location, and start year of operations is shown in Table 1. Coverage from each radar was available from the start year listed in Table 1. The radars begin operation on different dates and the data are not necessarily continuous due to maintenance or hardware issues.

The SuperDARN radars can operate in a multitude of different ways, scanning across the entire field of view, camping on a single beam, or weaving together more complicated scans from selected beams. The two scan programs that are used in this study are known as "common mode" and "two-f-sound". During common mode, the entire field of view is scanned at a one-minute resolution, moving from beam to beam sequentially and remaining at a fixed frequency. Two-f-sound mode is similar, however after each minute the radar switches between two different frequencies, which, in the case of this study, results in two different data sets at a two-minute resolution on separate frequencies.

2.2 Flow channel detection

SuperDARN data over a 6-year period (2010–2016) were used to identify radar scans containing fast flow channels.

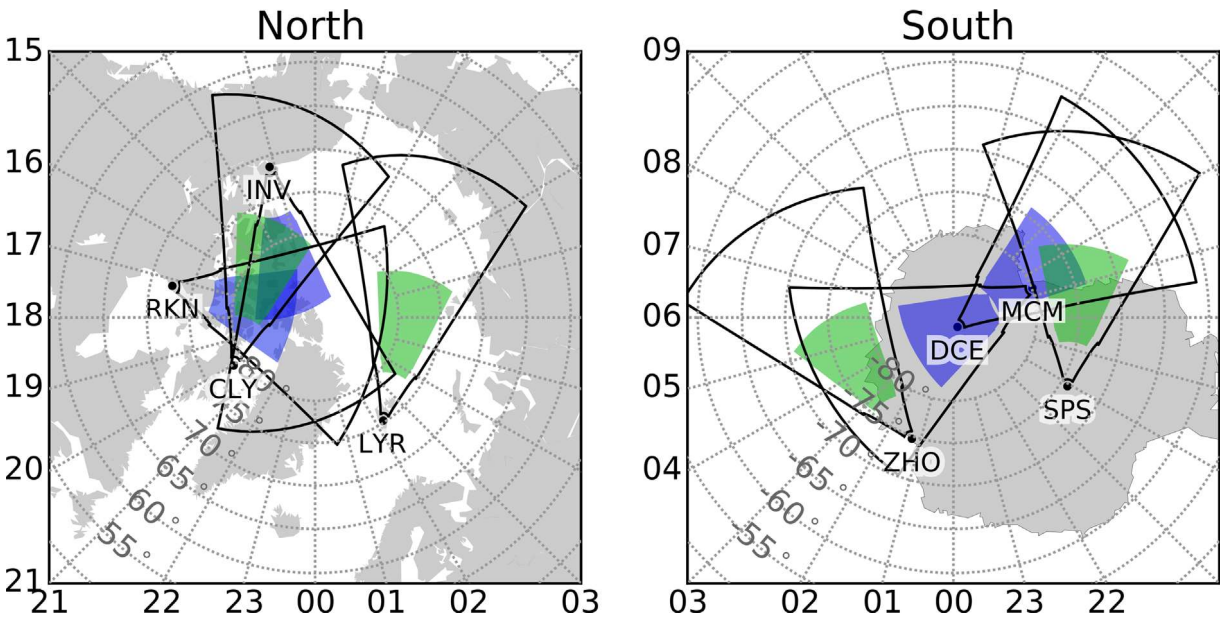

Figure 1. Map in magnetic local time/magnetic latitude coordinates of the SuperDARN radar locations and fields of view in (left) the Northern Hemisphere and (right) the Southern Hemisphere. The fields-of-view are colored green and blue in the 1/2 hop F-region if they are mostly zonally and meridionally orientated respectively. Further information about each radar is available in Table 1.

Table 1. Information about the SuperDARN radars used in this study. Geomagnetic locations are listed on the Virginia Tech SuperDARN website (http://vt.superdarn.org/tiki-index.php?page=Radar+Overview) and were calculated using 2005 AACGM coefficients with an assumed altitude of 100 km.

Station ID	Radar name	Hemisphere	Geomagnetic location	Start years
CLY	Clyde River	North	78.8° N 18.1° E	2012
INV	Inuvik	North	71.5° N −85.1° E	2008
RKN	Rankin Inlet	North	72.6° N −26.4° E	2008
LYR	Longyearbyen	North	74.9° N 127.6° E	2016
MCM	McMurdo	South	−80.0° N −33.3° E	2010
SPS	South Pole Station	South	−74.3° N 18.5° E	2013
ZHO	Zhongshan	South	−74.9° N 97.2° E	2010
DCE	Dome C	South	−88.9° N 54.6° E	2014

Eight different radars were used in this project, 4 in each hemisphere in the high-latitude North and South polar regions. The algorithm developed by Herlingshaw et al. (2019) was applied to the data to automatically detect the flow channels. This method targets structures with line-of-sight velocities over 900 m/s in magnitude, with sharp gradients (>400 m/s) between the high-speed flow channel and the slow-moving background flow on either side of the flow channel. This gradient change will occur over distances of 1 beam and/or range gate, depending on the orientation of the slice through the velocity of the flow channel. Principal component analysis and ellipse fitting were used to determine the width and orientation of the flow channel. An example of a detected flow channel is shown in Figure 2. Further information and examples of detected flow channels are available in Herlingshaw et al. (2019).

As the flow channel algorithm requires enough backscatter to detect the channel and a background flow on either side, 3 consecutive scans of common mode data are averaged together, which contains 3 min of data over a 3-minute interval. Only 2 sequential two-f-sound scans on each separate frequency are averaged together, which contain 2 min of data over a four-minute interval. This decision was made to keep the averaged scans as comparable as possible, with only a 1-minute difference in the extent of the data coverage. After detection, the flow channels were grouped into events, where a gap of $\geq$4 min without detection signified a new event. Parameters such as velocity, width, and location are then averaged over the event to gain one value for each flow channel. There is the possibility for flow channels to be double-counted in the statistics if they are detected on the same radar on both frequencies during the two-f-sound modes, or if they are detected by two radars in the same hemisphere at the same time. These instances have been located and removed from the data set.

2.3 AMPERE: open-closed boundary determination

The Active Magnetosphere and Planetary Electrodynamics Response Experiment (AMPERE) (Anderson et al., 2000) uses magnetic field data from the attitude control systems from the constellation of Iridium satellites. This is a network of approx-

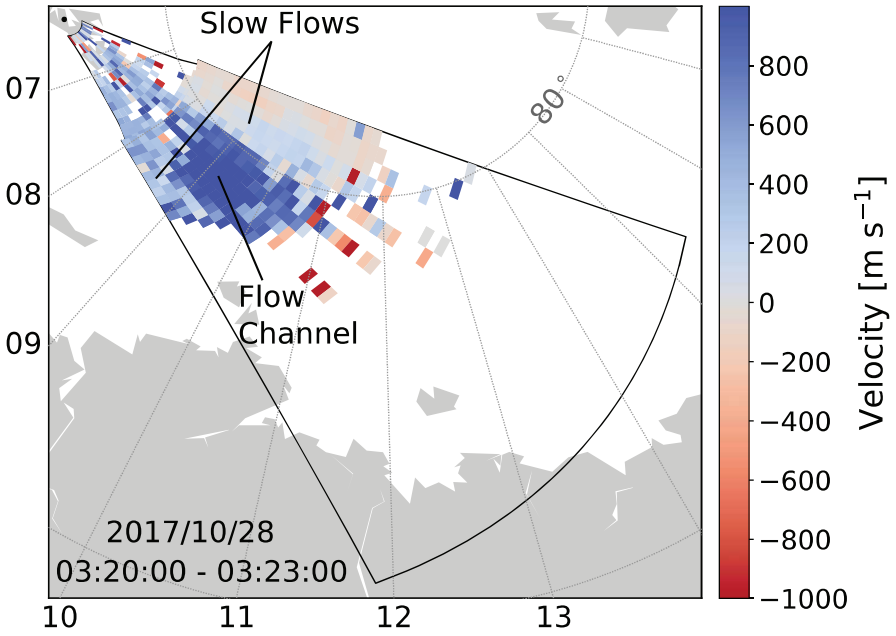

Figure 2. An example of a flow channel detected by the Longyearbyen radar that was identified using the flow channel detection algorithm developed by Herlingshaw et al. (2019).

imately 66 polar orbiting satellites at an altitude of 780 km in 6 different orbital planes with a longitudinal spacing of ~2 h of MLT and an orbital period of 104 min. A spherical harmonic fit is applied to the magnetic field data from the satellites and the curl of this is taken, effectively applying Ampere's law to the data and deriving the radial current density (Coxon et al., 2018). Current density maps of the polar regions, showing the large-scale Birkeland currents (region 1 and region 2) (Iijima & Potemra, 1976) can then be produced every 2 min, on a grid of 1° latitude and 1 h of MLT.

AMPERE data was used to determine if the majority of the detected flow channels were inside the polar cap. Milan et al. (2015) used a fitting routine on AMPERE current density maps to determine the boundary between the region 1 (R1) and region 2 (R2) bands of current. The available data cover the interval 2010–2016. The routine approximates this boundary as a circle and iterates between different circle center locations and radii, integrating the total current on the circle at each iteration. Positive and negative values represent upward and downward currents respectively. Currents located on the dawn side ($0 \leq \text{MLT} < 12$) are multiplied by -1, so that all R1 currents become positive, and all R2 currents become negative. A bipolar signature is then seen in the total integrated current with respect to the circle radius, maximizing in the positive (negative) sense at the location of R1 (R2). The boundary between the R1/R2 current systems is identified by the zero-crossing of the bipolar signature for the circle parameters that produce the largest peak-to-peak magnitude. Burrell et al. (2020) compared the R1/R2 boundary location to the open-closed field line boundary (OCB) location within data from the Defense Meteorological Satellite Program Special Sensor J (DMSP SSJ) electron energy flux. They found that the AMPERE R1–R2 boundary was shifted with respect to the OCB location by different amounts as a function of MLT. At noon/midnight, the AMPERE boundary lies 4°/2° equatorward of the OCB. In this study, the higher value of a 4° correction has been subtracted from the AMPERE circle radii so that it can function as a conservative OCB proxy. Events are therefore more likely to be within the true open field line boundary at all MLTs than if a 2° correction were used.

2.4 Interplanetary magnetic field data & dipole tilt angle

The IMF data were obtained from the NASA/GSFC's OMNI dataset through OMNIWeb at a 1-minute resolution (Papitashvili & King, 2020). The data have been shifted to the Earth's bow shock and the components of the magnetic field are given in Geocentric Solar Magnetospheric (GSM) coordinates.

To investigate the effects of different orientations of IMF on the flow channel distributions, it is useful to use the IMF clock angle (θ). This is defined as the angle between the geomagnetic north and the projection of the IMF vector onto the GSM Y–Z plane and is given by $\theta = \arctan(B_y, B_z)$, where θ ranges from 0° to 360°. A pure northward (positive B_z), dawnward (positive B_y), southward (negative B_z), and duskward IMF (negative B_y) are described by clock angles of 0°, 90°, 180°, and 270° respectively. The IMF was divided into different ranges to define positive IMF B_y dominant ($45° < \theta < 135°$) and negative IMF B_y dominant ($225° < \theta < 315°$) conditions.

For each of the flow channel events, the IMF conditions (average values of B_x, B_y, and B_z; the standard deviation of B_x, B_y, and B_z; IMF clock angle) were calculated using the preceding 1 h of OMNI IMF data. The period of 1 h was chosen to be consistent with previous studies investigating flows in the polar cap region (e.g. Bristow et al., 2015). A 1-hour interval helps to overcome propagation delay uncertainties from the measurement location of the satellite to the point at which the observed IMF begins to drive flows in the ionosphere.

The majority of the observed flow channels are driven only for short periods (~2–10 mins) within the dayside polar cap, therefore using longer intervals for the standard deviation could include the analysis of IMF variations that are unrelated to the driving of the flow channels.

A Monte Carlo simulation was used to obtain a suitable baseline of IMF conditions and dipole tilt angles with which to compare to those associated with the FC events. Using the OMNI IMF data from the years 2010–2016, a random selection of 30,000 times (which is comparable to the number of flow channels) was used to calculate average values of IMF B_x, B_y, and B_z as well as their standard deviation for 1 h prior to the selected times. In addition, the dipole tilt angle was calculated for the randomly selected times. This process was repeated 100 times, which resulted in values of IMF B_x, B_y, B_z, their standard deviations, and the dipole tilt angle with a sample size of ~3 million. This can be used to plot a probability distribution of the IMF conditions and dipole tilt angles which is representative of the entire distribution over the 6-year interval. The median of the MC-generated probability distributions of the standard deviation of IMF components was used to define stable (less than the median) and unstable (greater than the median) IMF conditions. These could then be used to determine if the FCs occurred under stable or unstable IMF conditions.

3 Results and analysis

In total, the algorithm detected 17,521 events with usable AMPERE fits over the 6-year period for all 8 radars. 7108 flow channels were detected in the Northern Hemisphere (NH) and 10,413 in the Southern Hemisphere (SH). In the years 2010–2016, the AMPERE boundary determination revealed that 79% of the flow channels occurred inside the polar cap and 21% occurred on closed field lines based on the AMPERE boundary determination described in Section 2.3. The flow channels equatorward of the AMPERE boundary (on closed field lines) have been removed from the statistics, as this study is concerned with polar cap flow channels on open field lines.

Figure 3 shows the magnetic latitude/magnetic local time (MLAT/MLT) occurrence distribution of the detected flow channels for the NH (Fig. 3a) and the SH (Fig. 3b). This figure shows that the highest number of flow channels were found on the dayside in both hemispheres. In the NH, there is a thick band of high occurrence (yellow bins) spanning from 77° to 83° in MLAT (6° wide) and 9–14 MLT. In the SH, there is a thinner band of high occurrence from 75° to 80° MLAT (5° wide) that stretches further around the dayside from 9 to 16 MLT. A thinner band of high occurrence also extends further around from 5 to 8 MLT. In both hemispheres, the flow channels were detected at all MLTs, with the lowest occurrences on the dusk flank and in the pre-midnight sector. On the nightside in the SH, there is a population of flow channels in the pre-midnight sector at 73–76°, which is an equatorward shift of approximately 3° compared to the dayside.

We note that there is a difference in the flow channel occurrence distributions in the NH and the SH (Fig. 3) that cannot be explained by gaps in radar coverage alone. The extent of FC 2 on the dawn flank (6–9 MLT) is concentrated in high occurrences between 80° and 82° in the NH, and between 76° and 79° in the SH. The low rate of flow channels above 80° in the SH can be explained by radar coverage gaps at the high latitudes. However, the lack of scatter equatorward of 80° on the dawn flank in the NH cannot be so easily explained as there is a high number of FC detections around noon down to 77°. This lack of detections is likely due to the coverage bias of radars with favorable field-of-views to detect flow channels on the flanks. Radars with zonally aligned field-of-views detect most of the scatter on the flanks as poleward-orientated radars will likely be mostly perpendicular to the mostly antisunward/sunward flows at these locations and therefore unable to measure the high line-of-sight velocities required for flow channel detection.

The ZHO and SPS radars measure the vast majority of flow channels on the flanks in the SH, and the CLY radar detects most in the NH. The LYR dataset (2016) is many years shorter than the CLY (2012–2016), so although this radar is zonally aligned it does not contribute significantly to the occurrence of flow channels on the flanks. The CLY field-of-view is not favorable for detecting scatter from less than 79°, as the flow channel must be located at the far ranges of the field-of-view, or in the most equatorward beams. Detections at these ranges would require ionospheric conditions to be favorable enough to support multi-hop propagation modes and the flow channel detection algorithm requires scatter on both sides of the channel, so it is most likely to detect the flow channels in the center of the field-of-view rather than on the edges. The radar fields-of-view in the NH with more meridional components (RKN and INV) have more favorable coverage to detect flow channels below 80°, especially closer to the radars (1/2 hop backscatter), and are responsible for the high occurrence of detections around noon below 80°. Occurrence distributions of the MLT/MLAT flow channel location for each radar are available in the Supplementary Material to support this discussion.

Figure 4 shows probability distributions for the IMF clock angle and the IMF B_y and B_z components, both for the flow channels and the Monte Carlo simulation probability distribution functions for typical IMF conditions. The clock angle distribution (Fig. 4a) shows that the MC and the flow channel distributions are generally IMF B_y dominant, peaking at angles ~90° (positive B_y directed) and 270° (negative B_y directed). However, the flow channel distribution shows higher occurrences than the MC distribution at IMF B_y dominant clock angles (peaking at 0.05 and 0.04 respectively), and lower occurrences than the MC distribution for IMF B_z dominant times. This suggests that flow channels are an IMF B_y dominant phenomena. The IMF B_y distribution (Fig. 4b) is essentially flat between −3 nT and 3 nT, whereas the flow channel distribution shows two clear peaks at ±3.5 nT. This suggests that flow channels preferentially occur for a higher than typical IMF B_y magnitude. The IMF B_z distribution (Fig. 4c) shows that although the IMF B_z component of the MC distribution is symmetrical around zero, the flow channel distribution shows a shift towards negative B_z, peaking at −0.5 nT. Flow channels have a preference for southward-directed IMF, occurring 57% of the time under southward conditions as opposed to 43% of the time for northward IMF. The distributions of IMF B_x for the flow channel and MC simulation were very similar. They showed lower magnitude discrepancies than in the IMF B_z distributions and thus were not included in the paper.

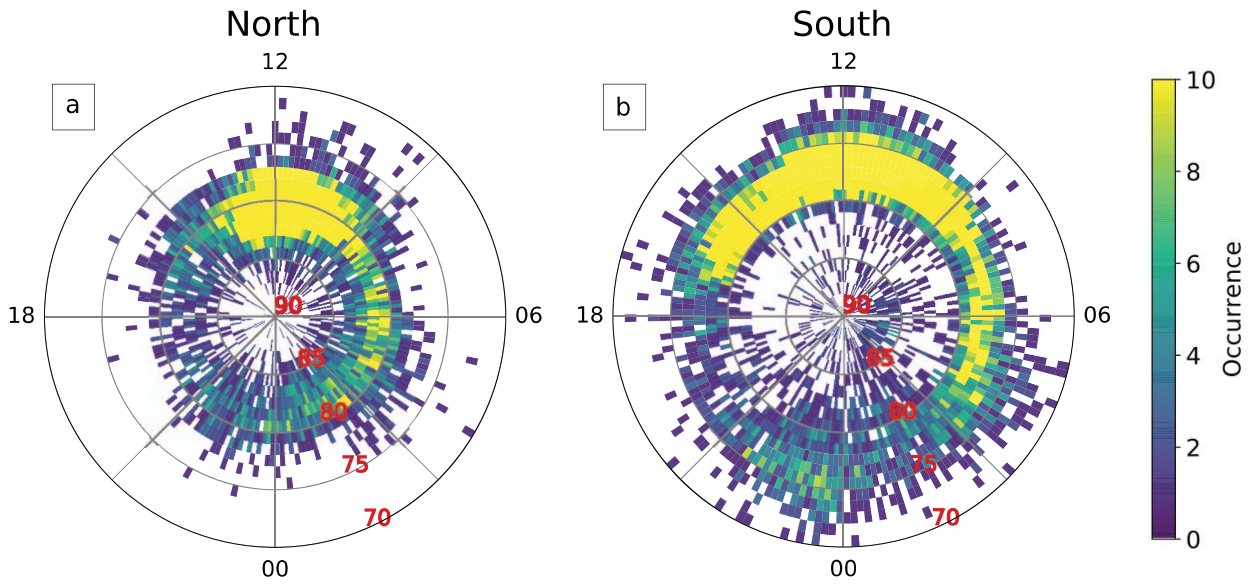

Figure 3. Flow channel occurrence distributions in magnetic latitude/magnetic local time (MLAT/MLT) for all 6 years of data for (a) the Northern Hemisphere and (b) the Southern Hemisphere. The location is based on the average location of the flow channel center during the event and binned in 1° MLAT by 8 min MLT bins and the occurrence in each cell represents the counts per bin.

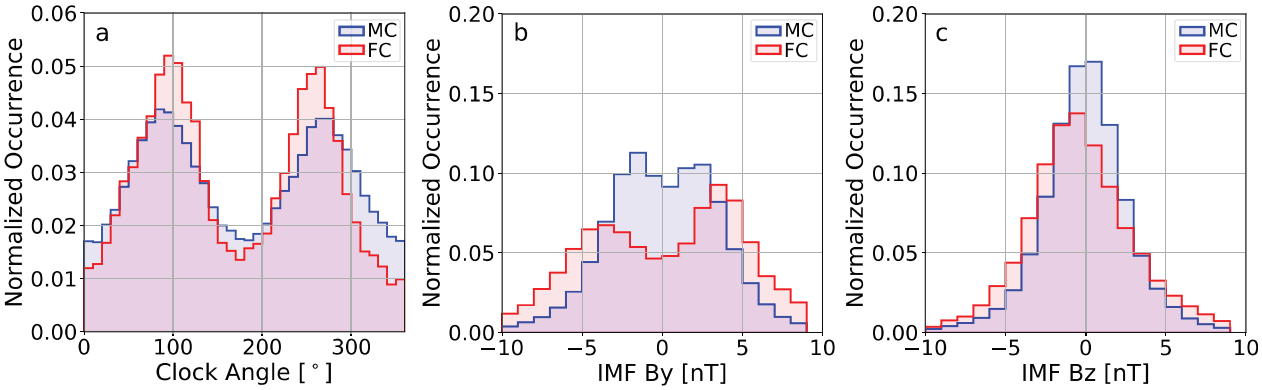

Figure 4. Probability distributions of the flow channel (FC, colored red) and Monte Carlo (MC, colored blue) for (a) the IMF clock angle, (b) the IMF B_y component, and (c) the IMF B_z component.

Figure 5 shows the IMF clock angle distribution for the NH and SH around noon (9–15 MLT), dawn (3–9 MLT), dusk (15–21 MLT), and midnight (21–3 MLT). The IMF clock angle was calculated as a 60-minute average before the flow channel start time. The flow channels detected around noon in both hemispheres (Fig. 5a) show a clear preference for B_y dominated conditions, peaking at clock angles close to 90° and 270°. There are very few channels for completely B_z-dominated IMF conditions (0° and 180°). However, particularly in the SH, the flow channels do not peak exactly at 90° and 270°, but slightly toward negative B_z dominant conditions. This suggests that most flow channels are observed under a dominant B_y component, with a preference for negative B_z, and suggests that the flow channels are generally reconnection-driven features. The distributions in each hemisphere are close to symmetrical, but slightly more events are present for positive IMF B_y in both hemispheres. At dawn (Fig. 5b), flow channels in the NH show a positive B_y preference, while in the SH a negative B_y preference is clear. At dusk (Fig. 5d), the reverse is true, with a negative B_y preference in the NH and a positive B_y preference in the SH. At midnight (Fig. 5c), an asymmetry is present and shows a B_y bias similar to that at dawn, but with a lower occurrence.

Figure 6 shows the MLT/MLAT distribution of the flow channel located in the Northern Hemisphere (top row) and the Southern Hemisphere (bottom row) under positive IMF B_y and negative B_y driving conditions. Convection equipotential contours have been overlaid in pink to add context to the observations. The TS18 model (Thomas & Shepherd, 2018) was used to calculate the contours with values of ±3.5 nT for B_y, −0.5 nT for B_z, and ±12.5° for the dipole tilt. These values were selected from the peaks of the distributions for the flow channels (Figs. 4 and 9). It should be noted that the TS18 model calculates values for the contours using NH data and assumes that the

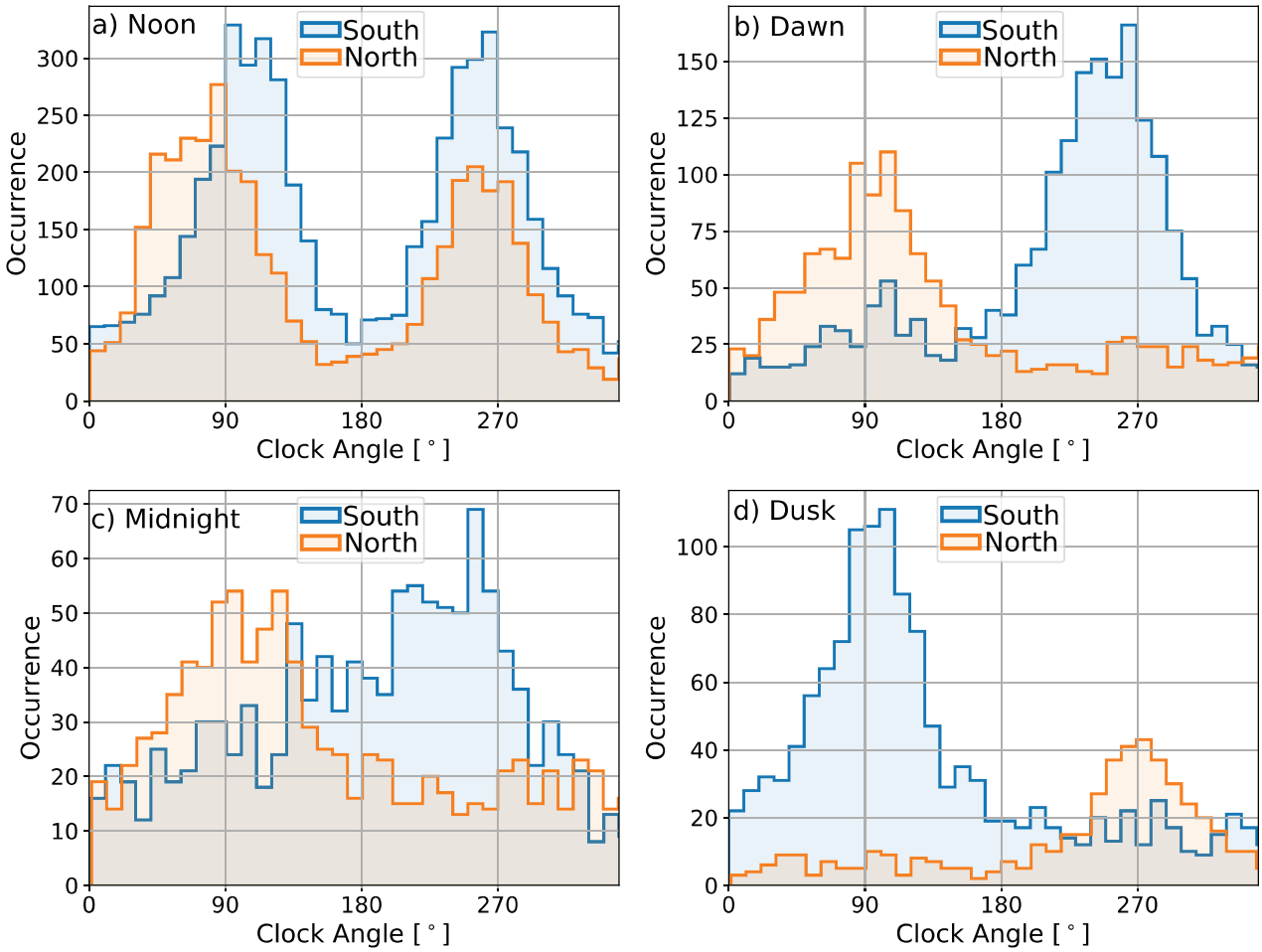

Figure 5. Histograms showing the clock angle distribution for the flow channel events in the Northern Hemisphere (orange) and the Southern Hemisphere (blue). The distributions are divided into MLT quadrants around (a) noon (9–15 MLT), (b) dawn (3–9 MLT), (c) midnight (21–3 MLT), and (d) dusk (15–21 MLT).

contours in the SH are mirror images. Figure 6a shows that under positive IMF B_y in the NH, the highest density of flow channel occurrence is shifted post-noon, with a region of lower occurrence stretching towards the dawn flank. Figure 6b shows that the opposite is true for negative IMF B_y in the NH, where the maximum occurrence is shifted towards the prenoon and the tail of the distribution stretches towards the dusk flank. This is the expected relation due to the releases in magnetic tension associated with IMF B_y. In the SH, the magnetic tension is opposite for each B_y orientation and the high occurrences begin in the prenoon (post-noon) sector for positive IMF B_y (negative IMF B_y) and extend around towards the dusk (dawn) flank. In the NH, the highest occurrence areas show a prominent spot shifted pre-/post-noon depending on the sign of IMF B_y, whereas in the SH this dayside feature is much broader in MLT.

Figures 7a–7c show the distributions of the standard deviations for IMF B_x, B_y, and B_z respectively. The flow channel distributions are colored red while the MC simulation results are colored blue. Black vertical lines indicate the median of the Monte Carlo distributions. Stable and unstable IMF conditions are defined to be below and above the median value respectively. The median values are 0.8 nT (B_x), 0.8 nT (B_y), and 1 nT (B_z). In all three distributions in Figure 7, the FC distribution is shifted towards higher standard deviations than the MC distributions, indicating that the flow channels occur under more unstable conditions than the MC simulation probability distribution. The percentage of flow channels that are unstable for each component is: 68% (B_x), 63% (B_y), and 69% (B_z). In 15% of cases, all three components were stable, while in 47% of cases, all three components were unstable, and in 38% of cases the components were a mixture of stable and unstable.

Figure 8 shows the MLAT/MLT distribution of flow channels for which all three components of the IMF up to 1 h prior to the flow channel were stable (Figs. 8a and 8c) and unstable (Figs. 8b and 8d) for the NH (top row) and the SH (bottom row). Over the 6-year interval, stable and unstable IMF conditions occur for the same percentage of the time. Consequently, the absolute occurrence of flow channels occurring under stable and unstable conditions in Figure 8 can then be directly compared. Both stable and unstable distributions in both hemispheres have the majority of flow channels concentrated in the dayside polar cap. Flow channels are more frequent at all MLTs for unstable IMF and there does not appear to be a distinct MLT/MLAT preference for flow channels occurring under stable and unstable conditions.

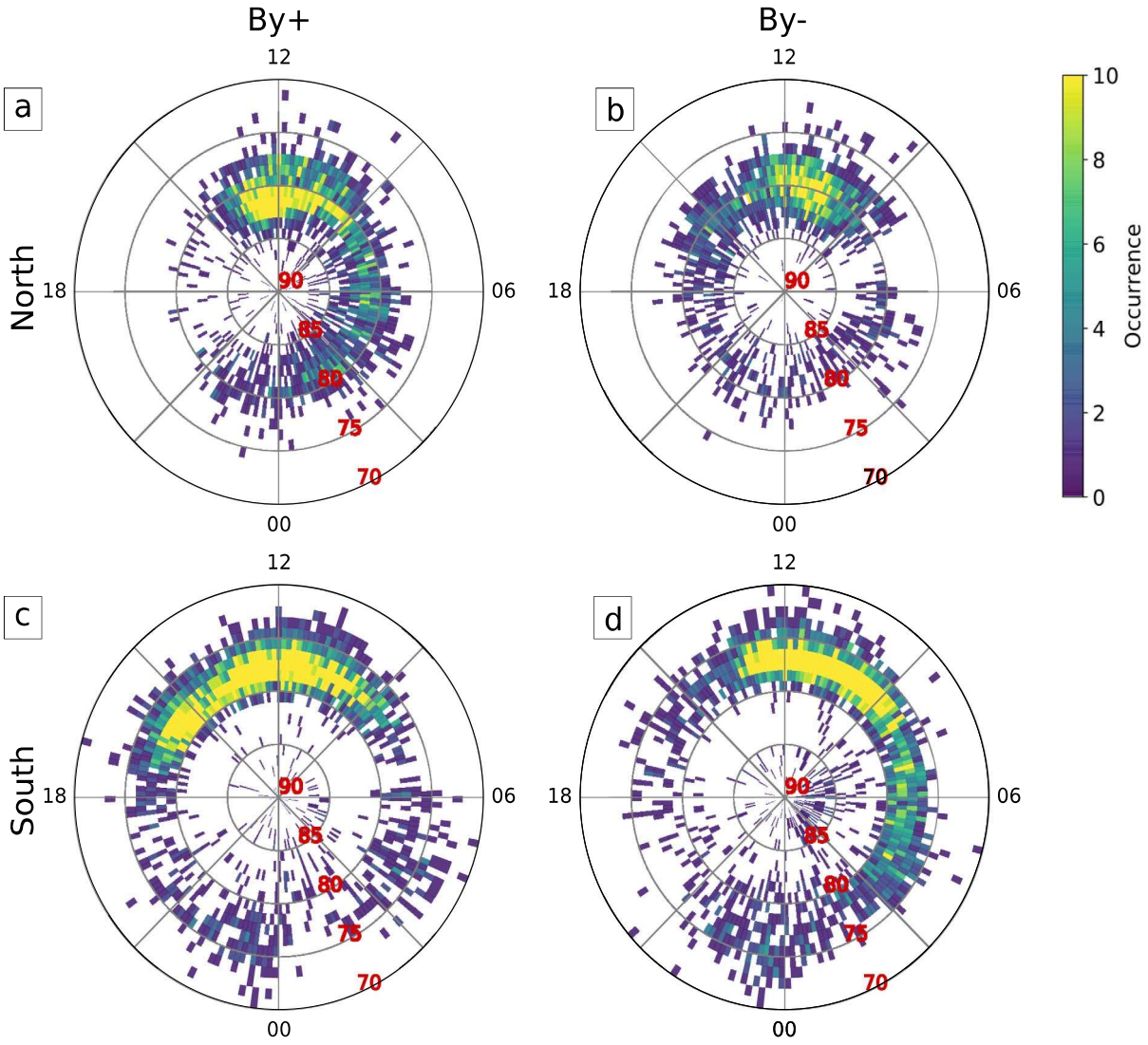

Figure 6. Flow channel event occurrence distributions in MLAT/MLT for(a) Northern Hemisphere under positive IMF B_y, (b) Northern hemisphere under negative IMF B_y, (c) Southern Hemisphere under positive IMF B_y, and (d) Southern Hemisphere under negative IMF B_y. The flow channel location is based on the average location of the flow channel center over the event and binned in 1° MLAT by 8 min MLT bins. Model convection cells have been overlaid in pink for context.

An analysis of the entire flow channel data set showed that the flow channels had an average width of ~300 km, average velocity magnitudes of ~1000 m/s, an average peak velocity of ~1400 m/s, and an average duration of ~5 min. These distributions are included in the Supplementary Material. Additionally, the solar wind velocity, IMF strength, and solar wind dynamic pressure driving conditions of flow channels were investigated. Compared to the MC simulation, FCs were found to have a slightly higher occurrence rate for above-average solar wind velocity, IMF strength, and solar wind dynamic pressure. However, a significant fraction (approximately 30–40%) of FCs are also observed during relatively low driving conditions. The flow channel yearly occurrence rates over the entire interval (2010–2016) were also studied to examine the possible effect of the solar cycle phase. During this interval, solar maximum occurred in 2014, with minimums occurring outside the window in 2008 and 2019. All of the radars showed the highest FC rates close to the solar maximum, which corroborates that slightly elevated solar wind velocity, magnetic field strength, and dynamic pressure are favorable, but not required, for the generation of FCs. The data discussed in this paragraph are not shown within the paper but are available in the Supplementary Material.

Figure 9 shows the probability distributions for both FC and the MC simulation for the dipole tilt angle in the NH (Fig. 9a) and the SH (Fig. 9b). The FCs have been filtered to select only those on the dayside ($18 < MLT < 6$) to investigate the source of the driving conditions of the dayside FCs. The MC distribution shows a symmetrical 2-peak distribution. These two peaks are likely an effect of the dipole tilt axis' yearly and daily variation. The dipole tilt angle for the flow channel distributions peaks at $-10°$ to $-15°$ in the NH and $+10°$ to $+15°$ in the SH. The flow channels are therefore observed more often between equinox and local winter.

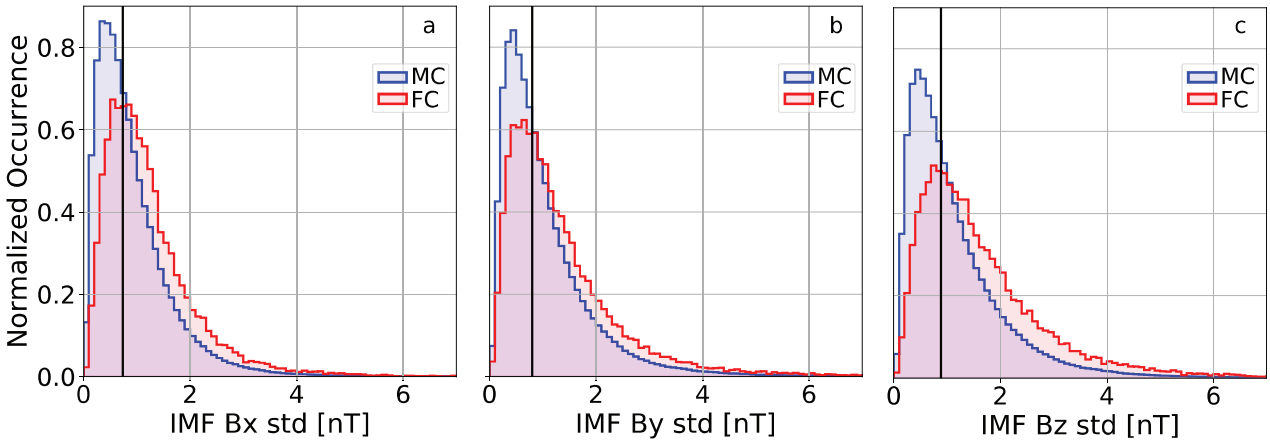

Figure 7. Normalized histograms of the standard deviation of the interplanetary magnetic field from the start of the flow channel event (labeled FC, colored red) and the Monte Carlo simulation (MC, colored blue) up to one hour prior for (a) IMF B_x, (b) IMF B_y, and (c) IMF B_z. Black vertical lines indicate the median values of the Monte Carlo distribution for each component.

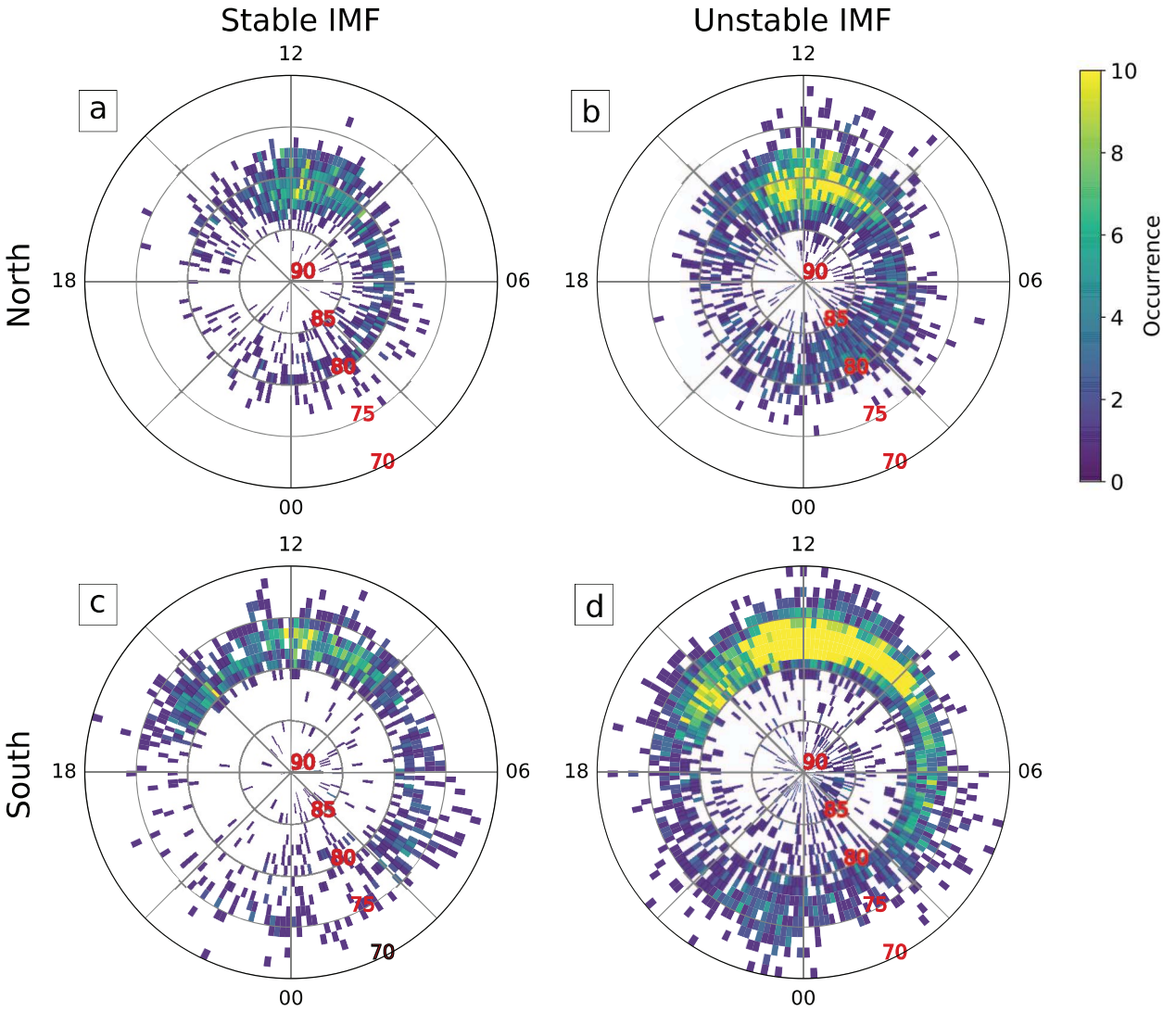

Figure 8. Flow channel event occurrence distributions in MLAT/MLT for the Northern Hemisphere (top row) and the Southern Hemisphere (bottom row) for stable IMF (left column) and unstable IMF (right column). The flow channel location is based on the average location of the flow channel center over the event and binned in 1° MLAT by 8 min MLT bins.

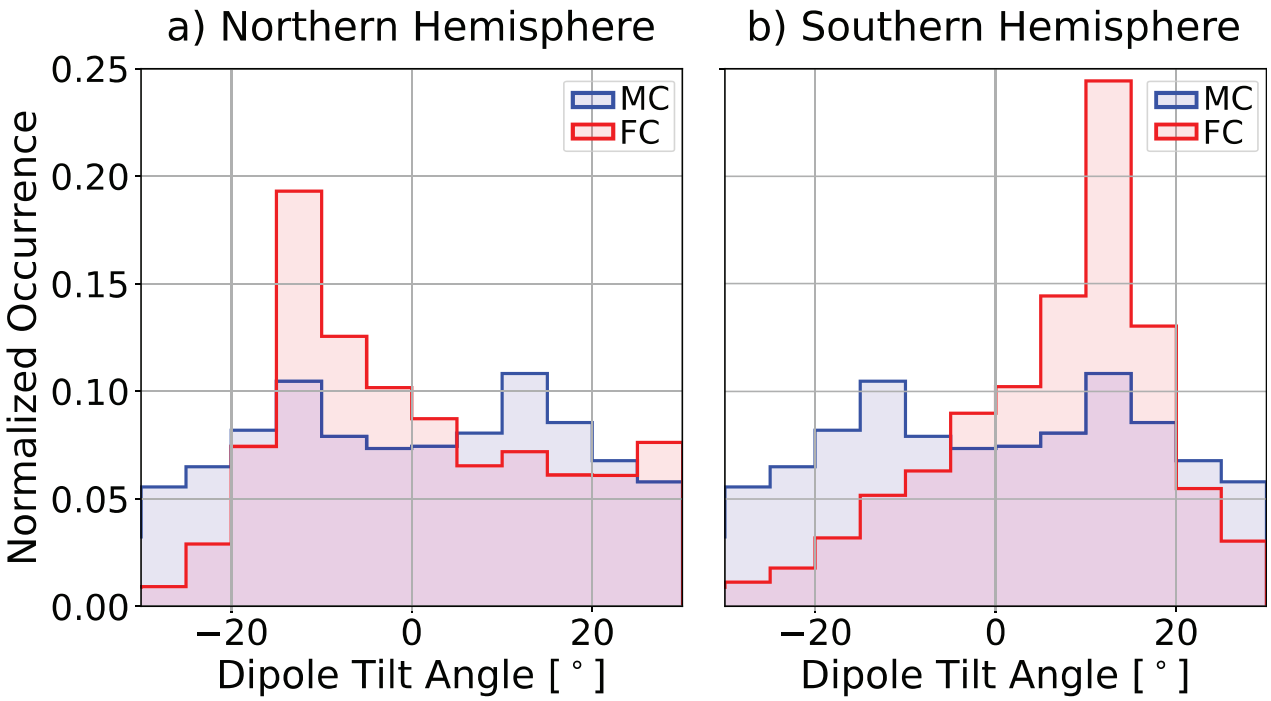

Figure 9. Probability distributions of the dipole tilt angle in (a) the Northern Hemisphere and (b) the Southern Hemisphere. The flow channel distribution is colored red and labeled FC. The Monte Carlo simulation shows an approximation of the probability distribution of the dipole tilt angle over the 6 year interval and is colored blue and labeled MC.

4 Discussion

In this study, a flow channel detection algorithm was applied to 6 years of SuperDARN data in the polar regions of both the Northern and Southern Hemispheres. The MLT/MLAT distribution of the flow channel location and its relationship to IMF driving conditions was extensively researched. This is the first time that flow channels within the polar caps have been studied over such a broad MLT/MLAT range and time span. It is also the first time that the IMF driving conditions of fast polar cap flow channels have been discussed statistically and they are found to occur frequently without requiring extreme values of IMF. This MLT/MLAT distribution also provides an interesting result as flow channels are not only detected on the dayside but also far around on the dawn and dusk flanks, a feature that has not been statistically researched before. A discussion of the results follows in the next sections.

4.1 Flow channel evolution

The majority of the detected flow channels occur on the dayside, as seen in Figure 3. The differences in the latitude of the distribution on the dayside are likely caused by the radar coverage distribution in each hemisphere. As seen in Figure 1, the radar layout in the NH has more coverage at the highest latitudes while the layout in the SH covers areas further equatorward with gaps in the highest latitude coverage. This could be the reason why the band of high occurrence spans from 77° to 85° in the NH, but is thinner and located at a lower latitude 76–80° in the SH. The flow channels surrounding noon (9–15 MLT) are classified as FC 1 within the S&F framework, occurring on newly-opened field lines. These flow channels have been previously observed in SuperDARN data within this area, or downstream of the dayside cusp region with similarly large flow speeds of 2–3 km/s (Pinnock et al., 1993), 900 m/s (Marchaudon et al., 2004), and 1 km/s (McWilliams et al., 2000).

These signatures are widely accepted to be the ionospheric response to flux transfer events within the magnetosphere (Neudegg et al., 2000). FC 1 occurs on newly-opened field lines and flow speeds can initially be very high due to the tension released as the field line re-configures. This could be why most of the events are observed within the 9–15 MLT dayside region in both hemispheres, as the 900 m/s threshold is high and requires strong magnetic tension forces to accelerate the plasma up to the detection threshold of the algorithm.

There is also a population of events stretching towards the flanks on the dayside, particularly on the dawnside. The flow channels on the dawn (6–9 MLT) and dusk (15–18 MLT) flanks of the polar cap fall within the FC 2 category within the S&F framework, occurring on old-open field lines that reconnected >10 min ago. These flow channels are no longer driven by the initial opening of flux due to dayside reconnection and are instead suggested to be caused by momentum transfer from field lines connected to the high-latitude boundary layer, tailwards of the cusp (Stern, 1984; Sandholt & Farrugia, 2009).

Although in the S&F framework flow channels on newly-opened and old-opened field lines are split into categories based on MLT ranges, it is perhaps not so simple to divide the two categories.

The nightside flow channels are detected in much smaller quantities than the dayside flow channels. These represent FC 3 and FC 4 in the S&F framework, which are flow channels linked to substorm activity and auroral streamers

(Sergeev et al., 1996; Andalsvik et al., 2012). Statistical studies (Wang et al., 2005) show that the most poleward latitudes of substorm onsets occur at 73° magnetic latitude. At the onset, the auroral oval will also expand, and auroral activity can occur polewards of the onset location. It is likely that the constraint of using the highest latitude SuperDARN radars leads to low occurrences of nightside driven flow channels, as their field-of-views extend no further equatorward than 60° in the SH and 65° in the NH. It is also difficult to observe scatter at the far ranges as this requires multiple-hop propagation. Propagation conditions have to be favorable to support these modes, and during auroral substorms, the ionosphere is very disturbed and can lead to decreases in backscatter at the radars (Wild & Grocott, 2008). The nightside flow channels are therefore less abundant in the statistics, and the algorithm (when applied to the radars in the polar regions) is more suitable for detecting dayside flow channels.

4.2 Flow channel dependence on IMF orientation

The majority of the observed fast-flow channels are driven by B_y dominated conditions. This can be inferred from Figure 5, as the distributions around all four of the quadrants peak at approximately 90° (positive B_y) and 270° (negative B_y). This B_y dependence has been observed in previous works, for example by Herlingshaw et al. (2020). However, the current study improves upon previous works as it uses multiple radars sampling in both the zonal and meridional directions. This suggests that the IMF B_y preference of flow channels cannot be explained as a bias in radar look direction and that an IMF B_y dominant component is more effective than a negative IMF B_z dominant component at accelerating the ionospheric plasma to the very fast flow speeds that the algorithm requires to register a detection. The asymmetries in the convection cells present under dominant IMF B_y conditions cause the preferences for flow channels under positive IMF B_y conditions at dawn and negative IMF B_y at dusk for the NH, with the opposite true for the SH. This preference cannot be explained by the general IMF B_y dominant nature of solar wind due to the Parker spiral, as the flow channels occur more frequently at IMF B_y dominant clock angles than the MC simulation probability distribution (Fig. 4).

Under IMF B_y dominant conditions, the flow channel location distribution is shifted pos-tnoon (prenoon) for positive IMF B_y (negative IMF B_y) conditions. The opposite sense is true in the SH, as is seen in Figure 6. This is the expected relation for flows on newly opened field lines under IMF B_y dominant conditions Herlingshaw et al. (2020). The convection throat differs from the flow channel feature itself as the convection throat can be over a broader area and the high-velocity flows within it have no minimum threshold velocity. The convection throat also does not have the constraint that the high-velocity flows should be embedded in a slower-moving background flow with a sharp gradient between the two. Another interesting feature in Figure 6 is the high occurrence of flow channels stretching towards the dawn flank for positive IMF B_y in the NH (Fig. 6a) and negative IMF B_y in the SH (Fig. 6d). This feature is also present at the dusk flank for negative IMF B_y in the NH (Fig. 6b) and positive IMF B_y in the SH (Fig. 6c), but it is not as well defined or as extensive, especially in the case of the NH.

The existence of fast flow channels on the dawn flank and their IMF B_y dependence agree with the work by Sandholt and Farrugia (2009). They used DMSP satellite passes to confirm the presence of these flow channels on old open field lines on the dawn and dusk flanks (FC 2). They found that the flow channels occurred on the dawn (dusk) flank for positive IMF B_y (negative IMF B_y) in the NH and for the opposite sense in the SH. This work was based on a series of case studies, as satellite passes were required. Our results here are the first time that FC 2 has been investigated in a statistical sense, and we find FC 2 to be a statistically significant feature in ionospheric circulation in both hemispheres on the dawn flank. FC 2 should also be visible on the dusk flank under negative IMF B_y in the NH and positive IMF B_y in the SH. The reason that the radars can detect FC 2 on the dawn flank may be due to the higher density plasma from the post-noon sector entering the polar cap during positive IMF B_y (NH) and negative IMF B_y (SH) conditions. This high-density plasma can result in more irregularities and therefore could create more favorable conditions for the radars to detect flow channels (Oksavik et al., 2010).

However, unlike Sandholt and Farrugia (2009) this study lacks information on the energies of the particles precipitating on the open field lines. Sometimes newly reconnected field lines can occur on extended *X*-lines, which can also stretch several hours of MLT around to the dawn or dusk flank. Most of the events in this study occur under non-extreme, smaller values of IMF B_y and a very slightly negative IMF B_z. Cases with an *X*-line that extends towards the dawn and dusk flanks have been documented to occur with higher than average components of IMF B_y or IMF B_z (or both) (Milan et al., 2000; Pinnock et al., 2003). Under smaller values of IMF B_y and B_z, the statistical region of newly reconnected field lines is narrower and concentrated closer to magnetic noon, spanning approximately 2 h of MLT (Newell et al., 2004). Therefore, from a statistical viewpoint, the majority of the FCs that are present on the flanks in this study are likely to be on old-open field lines, as they are far from this concentrated region around magnetic noon. However, without particle precipitation data it is not possible to conclusively decide whether the field lines are newly-opened and associated with energetic particle precipitation, or old-opened and associated with lower energy polar rain precipitation. This limits us to using the MLT ranges defined by Sandholt and Farrugia (2009) to distinguish different types of flow channels but provides an interesting area for future research with accompanying information on the incoming particle energies from satellite data. Examining the MLT/MLAT distribution, distance from the OCB, and energy spectra could help separate the flow channels into different categories of newly and old-open field lines more precisely than the MLT ranges proposed in the S&F framework.

4.3 Flow channel dependence on IMF stability & magnitude

Previous work investigating flow channels on the flanks of the polar cap on old open field lines has mainly been confined to times of constant, strong solar wind driving, such as during interplanetary coronal mass ejections (ICMEs) where the solar wind varies slowly over long periods of time with high magnitude components (Sandholt & Farrugia, 2009; Sandholt et al., 2010; Andalsvik et al., 2011). This was implemented to allow

polar cap passes from satellites under the same IMF conditions. Although FC 2 has been detected under stable conditions, whether this stability is a requirement for the formation of FC 2 has not been examined.

In this statistical study, a whole range of IMF conditions have been investigated, both low and high magnitudes and for stable and varying intervals. The sample of ~17,000 flow channels represents the most comprehensive statistics undertaken on flow channel IMF driving conditions to date. The distributions of the standard deviation in the IMF B_x, B_y, and B_z components 1 h before the flow channel start time were investigated in relation to Monte Carlo simulation probability distribution. The median of the Monte Carlo distribution for each component was used to split the FCs into stable (less than the median) and unstable (greater than the median) solar wind driving conditions.

The results from Figure 8 indicate that stable solar wind is not required to drive fast flow channels in the polar cap. The majority of the flow channels occur under unstable IMF conditions. The magnitude of IMF B_y in the lead-up to a flow channel is higher than the MC simulation probability distribution, peaking at ±3.5 nT, while IMF B_z shows a preference for southward IMF (peaking at −0.5 nT), as shown in Figure 4. These peak values are still low in magnitude compared to ICME conditions, which more typically have IMF B_y and B_z component magnitudes from 5 to 20 nT (Sandholt & Farrugia, 2009). The findings of this paper suggest that higher magnitudes of IMF B_y are preferred for flow channel formation, but extreme values are not required. The importance of understanding the role of the IMF B_y component in momentum transfer from the magnetosphere to the ionosphere has been highlighted by other recent studies. Interhemispheric asymmetries can be introduced by an IMF B_y component in the magnetosphere and ionosphere on both open and closed field lines (Svalgaard, 1968; Mansurov, 1969; Tenfjord et al., 2015). MHD simulations have revealed that the presence of an IMF B_y component can lead to a local B_y component in the closed magnetosphere within minutes through asymmetric loading and unloading of flux in the magnetotail lobes (Tenfjord et al., 2015, 2018). The results from this paper show that flow channels are most frequently observed for low-magnitude IMF conditions and therefore are a more common occurrence than previously observed. The localized strong flows associated with flow channels are likely to be significant mesoscale momentum and energy sources to the thermosphere through the ion-neutral coupling process (Deng et al., 2019). The contribution of flow channels to the estimation of energy deposition into the ionosphere is then possibly underestimated in current models and requires further study.

4.4 Interhemispheric asymmetries in flow channel occurrence

The Russell-McPherron effect, where the southward component becomes statistically more geoeffective at the equinoxes and there is a stronger coupling between the solar wind–magnetosphere–ionosphere system, should cause the FC occurrence distribution to peak at the spring and autumn equinoxes (Russell & McPherron, 1973). However, Figure 9 shows an asymmetry between the NH and the SH, where the FC occurrence peaks between the local winter and the equinox. This suggests that the FCs are not purely governed by solar wind–magnetosphere–ionosphere coupling efficiency. Ionospheric conductivity at high magnetic latitudes is on average largest in the summer, intermediate at the equinox, and smallest in winter (Cnossen et al., 2012). It could be that during winter, when the conductivity gradient between the auroral oval and polar cap is the largest, ionospheric flows can be funneled into a flow channel close to the boundary, especially in the case where there is another region of high conductivity on the polewards edge of the flow channel. One such case was noted by Herlingshaw et al. (2019), where a flow channel was located between a polar cap arc and the auroral oval boundary. An interplay of these two effects could then explain the location of the distributions peaking in-between equinox and local winter, as the flow channels require geomagnetic coupling to the solar wind driver (peaking at equinoxes) but is also dependent on conductivity gradients (largest in local winter). This could also explain the absence of a peak in summer, where conductivity in the polar cap is at its largest values and significant variation is not present as often to assist in funneling the flows into narrow channels. This topic requires further research, which could be explored with a combination of conductivity and convection velocity data and ionospheric simulation models.

Previous studies have shown a similar seasonal variation in overall SuperDARN echo rates. For example, the work of Koustov et al. (2019) shows approximately 3 times less F-region backscatter occurring during local summer in comparison to local winter and equinoxes over a selected portion of the fields-of-view of 6 polar cap radars. This study shows an approximate 4.5 times difference in the peak of the dipole tilt distribution between local winter and equinox and the value in local summer. The overall trends in occurrence rate could play a role in this distribution but perhaps not completely account for the significant difference in the dipole tilt angle distributions of the FCs in both hemispheres. There are significant differences in the area of the fields-of-view used in both studies and further investigation is required to clarify this matter, which is outside the scope of the current paper.

5 Conclusions

This study is the first large-scale, inter-hemispheric statistical study into ionospheric fast flow channels in the polar cap. An automatic flow channel detection algorithm developed by Herlingshaw et al. (2019) was applied to 6 years of SuperDARN data (2010–2016) to radars in the northern and southern polar cap regions. The distribution of these flow channels in MLT/MLAT was examined, and the solar wind driving conditions associated with the flow channels were studied. The main findings can be summarized as follows:

- 17,521 fast flow channel events in the polar cap were detected over 6 years, 7108 in the Northern Hemisphere, and 10,413 in the Southern Hemisphere.
- Fast flow channel events were detected at all MLTs with the majority of the fast flow channels found on the dayside in both hemispheres, and the lowest occurrences on the nightside and dusk flank. Dayside FC occurrences peaked between the local winter and equinox.

- The flow channel events show a preference for IMF B_y dominant solar wind driving conditions, with clock angle distributions peaking close to 90° and 270°.
- The flow channel events occur mainly under unstable IMF. The stability criterion was determined using a Monte Carlo simulation-based probability distribution of the standard deviation of the IMF components in randomly selected 1-hour intervals of IMF data.
- Under positive IMF B_y (negative IMF B_y) conditions in the Northern Hemisphere (Southern Hemisphere), flow channels are detected inside the polar cap on the dawn flank on old open field lines.
- Flow channels generally do not require large magnitudes of IMF B_y or IMF B_z to form, peaking in occurrence for magnitudes of ±3.5 nT for IMF B_y and −0.5 nT for IMF B_z.

We interpret these results as confirming statistically that fast flow channels with high magnitude flows (>900 m/s) and sharp gradients (>400 m/s) on either side show preferences for IMF B_y dominant, unstable IMF conditions. The fact that a significant population of flow channels is also observed on the dawn flank indicates the importance of M–I coupling mechanisms on most likely old open field lines, on the dawn/dusk flanks of the polar cap, away from the dayside and nightside reconnection regions.

Acknowledgements. Financial support was provided by the Research Council of Norway under contract 223252. We acknowledge the use of NASA/GSFC's Space Physics Data Facility's OMNIWeb (or CDAWeb or ftp) service, and OMNI data. The authors acknowledge the use of SuperDARN data, which are available online from the British Antarctic Survey (https://www.bas.ac.uk/project/superdarn), and thank Marina Schmidt and Kevin Krieger for their help accessing data. The authors would also like to thank Steve Milan for helpful discussions. SuperDARN is a collection of radars funded by the national scientific funding agencies of Australia, Canada, China, France, Italy, Japan, Norway, South Africa, the United Kingdom, and the United States of America. We thank the PIs of the radars used in this paper: Dag Lorentzen (University Centre in Svalbard) PI of the LYR radar, Kathryn McWilliams (University of Saskatchewan) PI of the CLY, SAS, and RKN radars, Bill Bristow (University of Alaska Fairbanks) PI of the MCM and SPS radars, Federica Marcucci (Institute for Space Astrophysics and Planetology) PI of the DCE radar, and Hongqiao Hu (Polar Research Institute of China) PI of the ZHO radar. We thank the AMPERE team and the AMPERE Science Center for providing the Iridiumâderived data products; AMPERE products are available at http://ampere.jhuapl.edu. We thank Steve Milan for providing the R1/R2 boundary circle fits from the AMPERE data, which are available online at https://leicester.figshare.com/articles/AMPERE_R1_R2_FAC_radii/11294861/1. The editor thanks William Bristow and an anonymous reviewer for their assistance in evaluating this paper.

Supplementary materials

The supplementary material of this article is available at https://www.swsc-journal.org/10.1051/swsc/2022037/olm.

Figure S1. Occurrence distributions of the MLT/MLAT flow channel location for each radar. The top row presents the distributions for the Northern Hemisphere for the Clyde River (CLY), Rankin Inlet (RKN), Inuvik (INV), and Longyearbyen (LYR) radars. The bottom row presents the distributions for the Southern Hemisphere for the Zhongshan (ZHO), South Pole Station (SPS), Dome C (DCE), and McMurdo (MCM) radars.

Figure S2. Histograms of the flow channel normalized distributions for (a) width (b) average (red) and peak (blue) velocity, and (c) duration.

Figure S3. A time series of the yearly flow channel occurrence for each of the radars, normalized to yearly operational radar time.

Figure S4. Histograms of the dayside flow channel (FC, colored red) and Monte Carlo (MC, colored blue) normalized distributions for (a) the IMF velocity, (b) the magnetic field strength, and (c) the solar wind dynamic pressure.

References

Andalsvik Y, Sandholt P, Farrugia C. 2011. Dayside and nightside contributions to cross-polar cap potential variations: the 20 March 2001 ICME case. *Ann Geophys* **29(11)**: 2189. https://doi.org/10.5194/angeo-29-2189-2011.

Andalsvik Y, Sandholt P, Farrugia C. 2012. Substorms and polar cap convection: the 10 January 2004 interplanetary CME case. *Ann Geophys* **30(1)**: 67–80. https://doi.org/10.5194/angeo-30-67-2012.

Anderson BJ, Takahashi K, Toth BA. 2000. Sensing global Birkeland currents with Iridium® engineering magnetometer data. *Geophys Res Lett* **27(24)**: 4045–4048. https://doi.org/10.1029/2000GL000094.

Birn J, Nakamura R, Panov E, Hesse M. 2011. Bursty bulk flows and dipolarization in MHD simulations of magnetotail reconnection. *J Geophys Res Space Phys* **116(A1)**. https://doi.org/10.1029/2010JA016083.

Bristow W, Amata E, Spaleta J, Marcucci M. 2015. Observations of the relationship between ionospheric central polar cap and dayside throat convection velocities, and solar wind/IMF driving. *J Geophys Res Space Phys* **120(6)**: 4684–4699. https://doi.org/10.1002/2015JA021199.

Burch J, Reiff P, Menietti J, Heelis R, Hanson W, Shawhan S, Shelley E, Sugiura M, Weimer D, Winningham J. 1985. IMF B_y-dependent plasma flow and Birkeland currents in the dayside magnetosphere: 1. Dynamics Explorer observations. *J Geophys Res Space Phys* **90(A2)**: 1577–1593. https://doi.org/10.1029/JA090iA02p01577.

Burrell AG, Chisham G, Milan SE, Kilcommons L, Chen Y-J, Thomas EG, Anderson B. 2020. AMPERE polar cap boundaries. *Ann Geophys* **38(2)**: 481–490. https://doi.org/10.5194/angeo-38-481-2020.

Chisham G, Lester M, Milan S, Freeman M, Bristow W, et al. 2007. A decade of the Super Dual Auroral Radar Network (SuperDARN): Scientific achievements, new techniques and future directions. *Surv Geophys* **28(1)**: 33–109. https://doi.org/10.1007/s10712-007-9017-8.

Cnossen I, Wiltberger M, Ouellette JE. 2012. The effects of seasonal and diurnal variations in the Earth's magnetic dipole orientation on solar wind–magnetosphere–ionosphere coupling. *J Geophys Res Space Phys* **117(A11)**: https://doi.org/10.1029/2012JA017825.

Cousins E, Shepherd S. 2010. A dynamical model of high-latitude convection derived from SuperDARN plasma drift measurements. *J Geophys Res Space Phys* **115(A12)**: https://doi.org/10.1029/2010JA016017.

Coxon JC, Milan SE, Anderson BJ. 2018. A review of Birkeland current research using AMPERE. In: *Electric Currents in Geospace and Beyond*, Keiling A, Marghitu O, Wheatland M (Eds.), Wiley, pp. 55–57. https://doi.org/10.1002/9781119324522.ch16.

Deng Y, Heelis R, Lyons LR, Nishimura Y, Gabrielse C. 2019. Impact of flow bursts in the auroral zone on the ionosphere and thermosphere. *J Geophys Res Space Phys* **124(12)**: 10459–10467. https://doi.org/10.1029/2019JA026755.

Dungey J. 1963. The structure of the exosphere, or adventures in velocity space, in: *Geophysics, The Earth's Environment*. deWitt C, Hieblot J, leBeau L (Eds.), Gordon and Breach, New York, pp. 505–550.

Dungey JW. 1961. Interplanetary magnetic field and the auroral zones. *Phys Rev Lett* **6(2)**: 47. https://doi.org/10.1103/PhysRevLett.6.47.

Farrugia C, Lund E, Sandholt P, Wild J, Cowley S, et al. 2004. Pulsed flows at the high-altitude cusp poleward boundary, and associated ionospheric convection and particle signatures, during a cluster-FAST-SuperDARN-sondrestrom conjunction under a southwest. *Ann Geophys* **22(8)**: 2891–2905. https://doi.org/10.5194/angeo-22-2891-2004.

Gabrielse C, Nishimura Y, Lyons L, Gallardo-Lacourt B, Deng Y, Donovan E. 2018. Statistical properties of mesoscale plasma flows in the nightside high-latitude ionosphere. *J Geophys Res Space Phys* **123(8)**: 6798–6820. https://doi.org/10.1029/2018JA025440.

Gallardo-Lacourt B, Nishimura Y, Lyons L, Zou S, Angelopoulos V, Donovan E, McWilliams K, Ruohoniemi J, Nishitani N. 2014. Coordinated SuperDARN THEMIS ASI observations of mesoscale flow bursts associated with auroral streamers. *J Geophys Res Space Phys* **119(1)**: 142–150. https://doi.org/10.1002/2013JA019245.

Greenwald R, Baker K, Dudeney J, Pinnock M, Jones T, et al. 1995. DARN/SUPERDARN: A global view of the dynamics of high-latitude convection. *Space Sci Rev* **71**: 761–796. https://doi.org/10.1007/BF00751350.

Haerendel G, Paschmann G, Sckopke N, Rosenbauer H, Hedgecock P. 1978. The frontside boundary layer of the magnetosphere and the problem of reconnection. *J Geophys Res Space Phys* **83(A7)**: 3195–3216. https://doi.org/10.1029/JA083iA07p03195.

Heelis R. 1984. The effects of interplanetary magnetic field orientation on dayside high-latitude ionospheric convection. *J Geophys Res Space Phys* **89(A5)**: 2873–2880. https://doi.org/10.1029/JA089iA05p02873.

Heppner J, Maynard N. 1987. Empirical high-latitude electric field models. *J Geophys Res Space Phys* **92(A5)**: 4467–4489. https://doi.org/10.1029/JA092iA05p04467.

Heppner JP. 1977. Empirical models of high-latitude electric fields. *J Geophys Res* **82(7)**: 1115–1125. https://doi.org/10.1029/JA092iA05p04467.

Herlingshaw K, Baddeley L, Oksavik K, Lorentzen D, Bland E. 2019. A study of automatically detected flow channels in the polar cap ionosphere. *J Geophys Res Space Phys* **124**: 9430–9447. https://doi.org/10.1029/2019JA026916.

Herlingshaw K, Baddeley L, Oksavik K, Lorentzen D, Bland E. 2020. A statistical study of polar cap flow channels and their IMF B_y dependence. *J Geophys Res Space Phys* **125**: https://doi.org/10.1029/2020JA028359.

Iijima T, Potemra TA. 1976. The amplitude distribution of field-aligned currents at northern high latitudes observed by Triad. *J Geophys Res* **81(13)**: 2165–2174. https://doi.org/10.1029/JA081i013p02165.

Koustov AV, Ullrich S, Ponomarenko PV, Nishitani N, Marcucci FM, Bristow WA. 2019. Occurrence of F region echoes for the polar cap SuperDARN radars. *Earth Planets Space* **71(1)**: 1–17. https://doi.org/10.1186/s40623-019-1092-9.

Lockwood M, Moen J, Cowley S, Farmer A, Løvhaug U, Lühr H, Davda V. 1993. Variability of dayside convection and motions of the cusp/cleft aurora. *Geophys Res Lett* **20(11)**: 1011–1014. https://doi.org/10.1029/93GL00846.

Lockwood M, Wild M. 1993. On the quasi-periodic nature of magnetopause flux transfer events. *J Geophys Res Space Phys* **98 (A4)**: 5935–5940. https://doi.org/10.1029/92JA02375.

Lu G, Richmond A, Emery B, Reiff P, de La Beaujardiere O, et al. 1994. Interhemispheric asymmetry of the high-latitude ionospheric convection pattern. *J Geophys Res Space Phys* **99(A4)**: 6491–6510. https://doi.org/10.1029/93JA03441.

Lyons L, Nishimura Y, Kim H-J, Donovan E, Angelopoulos V, Sofko G, Nicolls M, Heinselman C, Ruohoniemi J, Nishitani N. 2011. Possible connection of polar cap flows to pre-and post-substorm onset PBIs and streamers. *J Geophys Res Space Phys* **116(A12)**: https://doi.org/10.1029/2011JA016850.

Lyons L, Nishimura Y, Zou Y. 2016. Unsolved problems: Mesoscale polar cap flow channels' structure, propagation, and effects on space weather disturbances. *J Geophys Res Space Phys* **121(4)**: 3347–3352. https://doi.org/10.1002/2016JA022437.

Mansurov S. 1969. New evidence of a relationship between magnetic fields in space and on Earth. *Geomag Aeron* **9**: 622–623.

Marchaudon A, Cerisier J-C, Greenwald R, Sofko G. 2004. Electrodynamics of a flux transfer event: Experimental test of the Southwood model. *Geophys Res Lett* **31(9)**: https://doi.org/10.1029/2004GL019922.

Marklund G. 1984. Auroral arc classification scheme based on the observed arc-associated electric field pattern. *Planet Space Sci* **32(2)**: 193–211. https://doi.org/10.1016/0032-0633(84)90154-5.

McWilliams K, Yeoman T, Provan G. 2000. A statistical survey of dayside pulsed ionospheric flows as seen by the CUTLASS Finland HF radar. *Ann Geophys* **18(4)**: 445–453. https://doi.org/10.1007/s00585-000-0445-8.

Milan S, Carter J, Korth H, Anderson B. 2015. Principal component analysis of Birkeland currents determined by the active magnetosphere and planetary electrodynamics response experiment. *J Geophys Res Space Phys* **120(12)**: 10–415. https://doi.org/10.1002/2015JA021680.

Milan S, Lester M, Cowley S, Brittnacher M. 2000. Convection and auroral response to a southward turning of the IMF: Polar UVI, CUTLASS, and IMAGE signatures of transient magnetic flux transfer at the magnetopause. *J Geophys Res Space Phys* **105(A7)**: 15741–15755. https://doi.org/10.1029/2000JA900022.

Moen J, Carlson H, Oksavik K, Nielsen C, Pryse S, Middleton H, McCrea I, Gallop P. 2006. EISCAT observations of plasma patches at sub-auroral cusp latitudes. *Ann Geophys* **24(9)**: 2363–2374. https://doi.org/10.5194/angeo-24-2363-2006.

Moen J, Sandholt P, Lockwood M, Denig W, Løvhaug U, Lybekk B, Egeland A, Opsvik D, Friis-Christensen E. 1995. Events of enhanced convection and related dayside auroral activity. *J Geophys Res Space Phys* **100(A12)**: 23917–23934. https://doi.org/10.1029/95JA02585.

Neudegg D, Cowley S, Milan S, Yeoman TK, Lester M, et al. 2000. A survey of magnetopause FTEs and associated flow bursts in the polar ionosphere. *Ann Geophys* **18(4)**: 416–435. https://doi.org/10.1007/s00585-000-0416-0.

Newell P, Ruohoniemi J, Meng C-I. 2004. Maps of precipitation by source region, binned by IMF, with inertial convection streamlines. *J Geophys Res Space Phys* **109(A10)**: https://doi.org/10.1029/2004JA010499.

Nishimura Y, Lyons LR, Zou Y, Oksavik K, Moen J, et al. 2014. Day-night coupling by a localized flow channel visualized by polar cap patch propagation. *Geophys Res Lett* **41(11)**: 3701–3709. https://doi.org/10.1002/2014GL060301.

Nishitani N, Ruohoniemi JM, Lester M, Baker JBH, Koustov AV, et al. 2019. Review of the accomplishments of mid-latitude Super

Dual Auroral Radar Network (SuperDARN) HF radars. *Prog Earth Planet Sci* **6(1)**: 1–57. https://doi.org/10.1186/s40645-019-0300-3.

Oksavik K, Barth V, Moen J, Lester M. 2010. On the entry and transit of high-density plasma across the polar cap. *J Geophys Res Space Phys* **115(A12)**: https://doi.org/10.1029/2010JA015817.

Papitashvili N, King J. 2020. "OMNI 1-min data" IMF B_x, B_y, B_z, velocity, field strength, and dynamic pressure. *NASA Space Physics Data Facility*. https://doi.org/10.48322/45bb-8792. Accessed on 28 October 2022.

Pettigrew E, Shepherd S, Ruohoniemi J. 2010. Climatological patterns of high-latitude convection in the Northern and Southern hemispheres: Dipole tilt dependencies and interhemispheric comparisons. *J Geophys Res Space Phys* **115(A7)**: https://doi.org/10.1029/2009JA014956.

Pinnock M, Chisham G, Coleman I, Freeman M, Hairston M, Villain J-P. 2003. The location and rate of dayside reconnection during an interval of southward interplanetary magnetic field. *Ann Geophys* **21(7)**: 1467–1482. https://doi.org/10.5194/angeo-21-1467-2003.

Pinnock M, Rodger AS, Dudeney J, Baker K, Newell P, Greenwald R, Greenspan M. 1993. Observations of an enhanced convection channel in the cusp ionosphere. *J Geophys Res Space Phys* **98(A3)**: 3767–3776. https://doi.org/10.1029/92JA01382.

Provan G, Yeoman T, Cowley S. 1999. The influence of the IMF B_y component on the location of pulsed flows in the dayside ionosphere observed by an HF radar. *Geophys Res Lett* **26(4)**: 521–524. https://doi.org/10.1029/1999GL900009.

Provan G, Yeoman T, Milan S. 1998. CUTLASS Finland radar observations of the ionospheric signatures of flux transfer events and the resulting plasma flows. *Ann Geophys* **16(11)**: 1411–1422. https://doi.org/10.1007/s00585-998-1411-0.

Rich FJ, Hairston M. 1994. Large-scale convection patterns observed by DMSP. *J Geophys Res Space Phys* **99(A3)**: 3827–3844. https://doi.org/10.1029/93JA03296.

Ruohoniemi J, Greenwald R. 1996. Statistical patterns of high-latitude convection obtained from Goose Bay HF radar observations. *J Geophys Res Space Phys* **101(A10)**: 21743–21763. https://doi.org/10.1029/96JA01584.

Ruohoniemi J, Greenwald R. 2005. Dependencies of high-latitude plasma convection: Consideration of interplanetary magnetic field, seasonal, and universal time factors in statistical patterns. *J Geophys Res Space Phys* **110(A9)**: https://doi.org/10.1029/2004JA010815.

Russell C, McPherron R. 1973. Semiannual variation of geomagnetic activity. *J Geophys Res* **78(1)**: 92–108. https://doi.org/10.1029/JA078i001p00092.

Russell CT, Elphic R. 1978. Initial ISEE magnetometer results: Magnetopause observations. *Space Sci Rev* **22(6)**: 681–715. https://doi.org/10.1007/BF00212619.

Russell CT, Elphic R. 1979. ISEE observations of flux transfer events at the dayside magnetopause. *Geophys Res Lett* **6(1)**: 33–36. https://doi.org/10.1029/GL006i001p00033.

Sandholt P, Andalsvik Y, Farrugia C. 2010. Polar cap convection/precipitation states during Earth passage of two ICMEs at solar minimum. *Ann Geophys* **28(4)**: 1023–1042. https://doi.org/10.5194/angeo-28-1023-2010.

Sandholt P, Farrugia C. 2007. Role of poleward moving auroral forms in the dawn-dusk auroral precipitation asymmetries induced by IMF B_y. *J Geophys Res Space Phys* **112(A4)**: https://doi.org/10.1029/2006JA011952.

Sandholt P, Farrugia C. 2009. Plasma flow channels at the dawn/dusk polar cap boundaries: Momentum transfer on old open field lines and the roles of IMF B_y and conductivity gradients. *Ann Geophys* **27(4)**: 1527–1554. https://doi.org/10.5194/angeo-27-1527-2009.

Sandholt P, Farrugia C, Denig W. 2004. Detailed dayside auroral morphology as a function of local time for southeast IMF orientation: Implications for solar wind-magnetosphere coupling. *Ann Geophys* **22(10)**: 3537–3560. https://doi.org/10.5194/angeo-22-3537-2004.

Sergeev V, Angelopoulos V, Gosling J, Cattell C, Russell C. 1996. Detection of localized, plasma-depleted flux tubes or bubbles in the midtail plasma sheet. *J Geophys Res Space Phys* **101(A5)**: 10817–10826. https://doi.org/10.1029/96JA00460.

Stern DP. 1984. Magnetospheric dynamo processes. In: *Magnetospheric Currents*, Potemra TA (Ed.), Wiley Online Library. https://doi.org/10.1029/GM028p0200.

Svalgaard L. 1968. Sector structure of the interplanetary magnetic field and daily variation of the geomagneticfield at high latitudes, Paper 6, *Danish Meteorological Inst. Geophysics*, Charlottenlund, Denmark.

Tenfjord P, Østgaard N, Haaland S, Snekvik K, Laundal K, Reistad J, Strangeway R, Milan S, Hesse M, Ohma A. 2018. How the IMF B_y induces a local B_y component during northward IMF B_z and characteristic timescales. *J Geophys Res Space Phys* **123(5)**: 3333–3348. https://doi.org/10.1002/2018JA025186.

Tenfjord P, Østgaard N, Snekvik K, Laundal KM, Reistad JP, Haaland S, Milan S. 2015. How the IMF B_y induces a B_y component in the closed magnetosphere and how it leads to asymmetric currents and convection patterns in the two hemispheres. *J Geophys Res Space Phys* **120(11)**: 9368–9384. https://doi.org/10.1002/2015JA021579.

Thomas EG, Shepherd SG. 2018. Statistical patterns of ionospheric convection derived from mid-latitude, high-latitude, and polar SuperDARN HF radar observations. *J Geophys Res Space Phys* **123(4)**: 3196–3216. https://doi.org/10.1002/2018JA025280.

Wang H, Lühr H, Ma S, Ritter P. 2005. Statistical study of the substorm onset: its dependence on solar wind parameters and solar illumination. *Ann Geophys* **23(6)**: 2069–2079. https://doi.org/10.5194/angeo-23-2069-2005.

Wang H, Lühr H, Ridley AJ. 2010. Plasma convection jets near the poleward boundary of the nightside auroral oval and their relation to Pedersen conductivity gradients. *Ann Geophys* **28(4)**: 969–976. https://doi.org/10.5194/angeo-28-969-2010.

Wild JA, Grocott A. 2008. The influence of magnetospheric substorms on SuperDARN radar backscatter. *J Geophys Res Space Phys* **113(A4)**: https://doi.org/10.1029/2007JA012910.

Zou Y, Nishimura Y, Lyons L, Donovan E, Ruohoniemi J, Nishitani N, McWilliams K. 2014. Statistical relationships between enhanced polar cap flows and PBIs. *J Geophys Res Space Phys* **119(1)**: 151–162. https://doi.org/10.1002/2013JA019269.

Zou Y, Nishimura Y, Lyons LR, Donovan EF, Shiokawa K, Ruohoniemi JM, McWilliams KA, Nishitani N. 2015. Polar cap precursor of nightside auroral oval intensifications using polar cap arcs. *J Geophys Res Space Phys* **120(12)**: 10–698. https://doi.org/10.1002/2015JA021816.

Cite this article as: Herlingshaw K, Baddeley L, Oksavik K, Lorentzen DA & Laundal KM. 2022. A statistical study of polar cap flow channels observed in both hemispheres using SuperDARN radars. *J. Space Weather Space Clim.* **12**, 39. https://doi.org/10.1051/swsc/2022037.